ELSEVIER

Journal of Quantitative Spectroscopy & Radiative Transfer 95 (2005) 539–556

Journal of Quantitative Spectroscopy & Radiative Transfer

www.elsevier.com/locate/jqsrt

Application of principal component analysis to high spectral resolution radiative transfer: A case study of the O_2 A band

Vijay Natraj[a,*], Xun Jiang[a], Run-lie Shia[a], Xianglei Huang[b], Jack S. Margolis[c], Yuk L. Yung[a]

[a]*Division of Geological and Planetary Sciences, California Institute of Technology, MC 150-21, 1200 E. California Blvd., Pasadena, CA 91125, USA*

[b]*Program in Atmospheric and Oceanic Sciences, Princeton University, Princeton, NJ 08544, USA*

[c]*RSA Systems, 2235 N. Lake Ave. #207, Altadena, CA 91101, USA*

Received 28 September 2004; accepted 12 December 2004

Abstract

Radiative transfer computation is the rate-limiting step in most high spectral resolution remote sensing retrieval applications. While several techniques have been proposed to speed up radiative transfer calculations, they all suffer from accuracy considerations. We propose a new method, based on a principal component analysis of the optical properties of the system, that addresses these concerns. Taking atmospheric transmission in the O_2 A band as a test case, we reproduced the reflectance spectrum at the top of the atmosphere (TOA), obtained using the multiple scattering code DISORT, with an accuracy of 0.3%, while achieving an order of magnitude improvement in speed.

Keywords: Radiative transfer; Principal component analysis; Empirical orthogonal function; Remote sensing; Retrieval; O_2 A band

*Corresponding author. Tel.: +1 626 796 4557; fax: +1 626 585 1917.
E-mail address: vijay@gps.caltech.edu (V. Natraj).

0022-4073/$ - see front matter © 2005 Elsevier Ltd. All rights reserved.
doi:10.1016/j.jqsrt.2004.12.024

1. Introduction

It is well known that the computation of radiative transfer is the bottleneck in remote sensing retrieval problems. The timely retrieval of atmospheric trace gas concentrations from space-borne spectral measurements of radiation reflected through the earth's atmosphere [1] requires computationally efficient sampling techniques in order to accurately model the spectral absorption and scattering signatures of the gases under study.

The first applications of spectral sampling techniques to atmospheric modeling date back to the 1930s (see [2] for an historical account). Since then such techniques have been improved a great deal. A popular scheme is the k-distribution method, which involves grouping spectral intervals according to absorption coefficient (k) strength ([3–7]). An extension of this method is the correlated k-distribution method, by which the frequency order of absorption coefficients for one gas rearranged by strength at one altitude is the same as that at another ([8–12]).

The drawback of the correlated k-distribution method is that it assumes that atmospheric optical properties are spectrally correlated at all points along the optical path, such that spectral intervals with similar optical properties at one level of the atmosphere will remain similar at all other levels. This assumption is rigorously valid for homogeneous, isobaric, isothermal optical paths, but it usually breaks down for realistic inhomogeneous, non-isothermal, atmospheric optical paths. This loss of correlation can sometimes introduce significant radiance errors.

Spectral mapping methods [13,14] have also been proposed to enhance computational speed. Like the correlated k-distribution method, spectral mapping methods gain their efficiency by identifying spectral intervals that have similar optical properties. These intervals are then gathered into bins, and a single monochromatic multiple scattering calculation can be performed for each bin. Spectral mapping methods make no assumptions about the spectral correlation along the optical path. Instead, these methods perform a level-by-level comparison of monochromatic atmospheric and surface optical properties, and combine only those spectral regions that actually remain in agreement at all points along the inhomogeneous optical path. The disadvantage here is that fine spectral binning is required to maintain accuracy in the radiative transfer calculation, but this results in minimal gains in computational efficiency and comes at the expense of a significantly more complex retrieval code. Coarse spectral binning, on the other hand, provides excellent computational efficiency increases at the expense of significant reduction in the accuracy of the calculated radiances. Also, since different bins are used for the calculation of the base state and the perturbed state (when doing finite difference partial differentiation), there are discontinuities in the partial derivatives.

Thus, there is clearly a need for an alternative scheme that does not compromise on accuracy while enhancing computational efficiency.

2. Model description

In our analysis, we seek an accurate and efficient characterization of near-infrared (NIR) absorption in the O_2 A band centered at 760 nm. O_2 A band observations can provide surface pressure estimates with accuracies of $\sim$1 mbar [15]. The presence of strong and weak absorption lines also makes it useful for characterizing the vertical distribution of clouds and aerosols [16].

We use a 23-level model atmosphere, obtained from the ECMWF data for a sub-tropical northern hemisphere (15°N) summer (http://data.ecmwf.int/data/d/era40_daily/), with 15 levels in the stratosphere and the remaining in the troposphere (see Table 1 for details). The levels are spaced linearly in log(pressure) from 1 mbar to 1 bar. Rayleigh scattering by air molecules and scattering by aerosols are taken into account. High altitude cirrus is not considered here, but will be in a following paper in view of its potential importance in remote sensing retrievals. The total aerosol optical depth and the surface albedo are assumed to be 0.05 and 0.2, respectively. Varying the aerosol optical depth distribution had negligible impact on both the qualitative nature of the empirical orthogonal functions (EOFs) and the error in reproducing the O_2 A band spectrum. The spectroscopic data are taken from the HITRAN2K line list [17].

3. Multiple scattering codes

Two codes were used to generate the O_2 A band spectrum: the multi-stream, line-by-line multiple scattering code DISORT [18], and a multiple scattering code which uses only two streams (one up, one down), to be henceforth called TWOSTR [19]. DISORT and TWOSTR, which are extremely well tested and documented, are available for download from the NASA Goddard website ftp://climate.gsfc.nasa.gov/wiscombe/Multiple_Scatt/. A report that describes the features of DISORT and explains its usage can also be found there.

DISORT is on average two to three orders of magnitude slower than TWOSTR. Fig. 1 shows the reflectance spectrum obtained from DISORT at the top of the atmosphere (TOA), the correlation between the DISORT and scaled TWOSTR spectra, and the difference between the two calculations. The scaling of the TWOSTR spectrum is done as follows:

A least squares fit is done to the DISORT and TWOSTR reflectances to find the linear regression coefficients m (slope) and c (y-intercept), i.e.

$$\text{TWOSTR\_FITTED} = m\,\text{DISORT} + c. \tag{1}$$

The scaled TWOSTR reflectances (hereafter the word *scaled* is dropped) are then obtained using

$$\text{TWOSTR\_SCALED} = \frac{\text{TWOSTR} - c}{m}. \tag{2}$$

It is clear that the TWOSTR spectrum has a very good correlation with that from DISORT. Let $D(i)$ and $T(i)$ be the reflectances produced by DISORT and TWOSTR, respectively, at the ith wavenumber. We observe that $D(j) - D(k)$ is much larger than $[D(j) - T(j)] - [D(k) - T(k)]$, where j and k are any two wavenumbers. In other words, the variance is much lower for the residual than for the reflectances directly obtained from DISORT. As explained in Section 5, this feature is exploited by performing principal component (PC) analysis on the *residual* between DISORT and TWOSTR reflectances. Our method combines the strengths of PC analysis and the TWOSTR radiative transfer model. The P and R branches of the O_2 A band were considered separately because of the different line shapes in each branch, due to line mixing in the R branch.

Table 1
Model atmosphere

Level	Pressure (hPa)	Temperature (K)	O_2 mass mixing ratio
0	1.000×10^0	262.5	0.234
1	1.369×10^0	260.6	0.233
2	1.874×10^0	257.0	0.234
3	2.565×10^0	251.5	0.234
4	3.511×10^0	245.1	0.234
5	4.806×10^0	240.2	0.233
6	6.579×10^0	236.5	0.232
7	9.006×10^0	233.2	0.233
8	1.233×10^1	229.9	0.234
9	1.688×10^1	226.4	0.233
10	2.310×10^1	222.8	0.233
11	3.162×10^1	218.7	0.232
12	4.329×10^1	213.9	0.232
13	5.926×10^1	208.2	0.232
14	8.111×10^1	202.7	0.233
15	1.110×10^2	201.8	0.232
16	1.520×10^2	209.9	0.229
17	2.081×10^2	222.9	0.232
18	2.848×10^2	238.6	0.233
19	3.899×10^2	254.7	0.231
20	5.337×10^2	269.8	0.231
21	7.305×10^2	285.7	0.230
22	1.000×10^3	300.1	0.231

The pressure, temperature and mixing ratio are level quantities. The corresponding layer values are assumed to be the mean of the values at the levels bounding the layer. Level 0 is the TOA and level 22 refers to the surface.

4. Empirical orthogonal functions (EOFs)

A good discussion of PC analysis can be found in Huang et al. [20] and Camp et al. [21]. Peixoto and Oort [22] give an excellent physical and mathematical interpretation, in Section 4.3 and Appendix B, respectively, of their book *Physics of Climate*. Here the data set consists of s optical properties in M atmospheric layers at N wavenumbers, denoted by F_{il}, where i varies from 1 to sM and l varies from 1 to sN. The EOFs, $\boldsymbol{\varphi}_k$, $k = 1, \ldots, sM$, are unit eigenvectors of the mean-removed covariance matrix $\mathbf{C}$ (of dimension $sM \times sM$) whose elements are given by

$$C_{ij} = \overline{(F_{il} - \overline{F_i})(F_{jl} - \overline{F_j})}, \tag{3}$$

where the overbar denotes an average over all wavenumbers. The variance associated with the kth EOF, V_k, is obtained from the diagonal elements of $\mathbf{C}$.

$$V_k = C_{kk}. \tag{4}$$

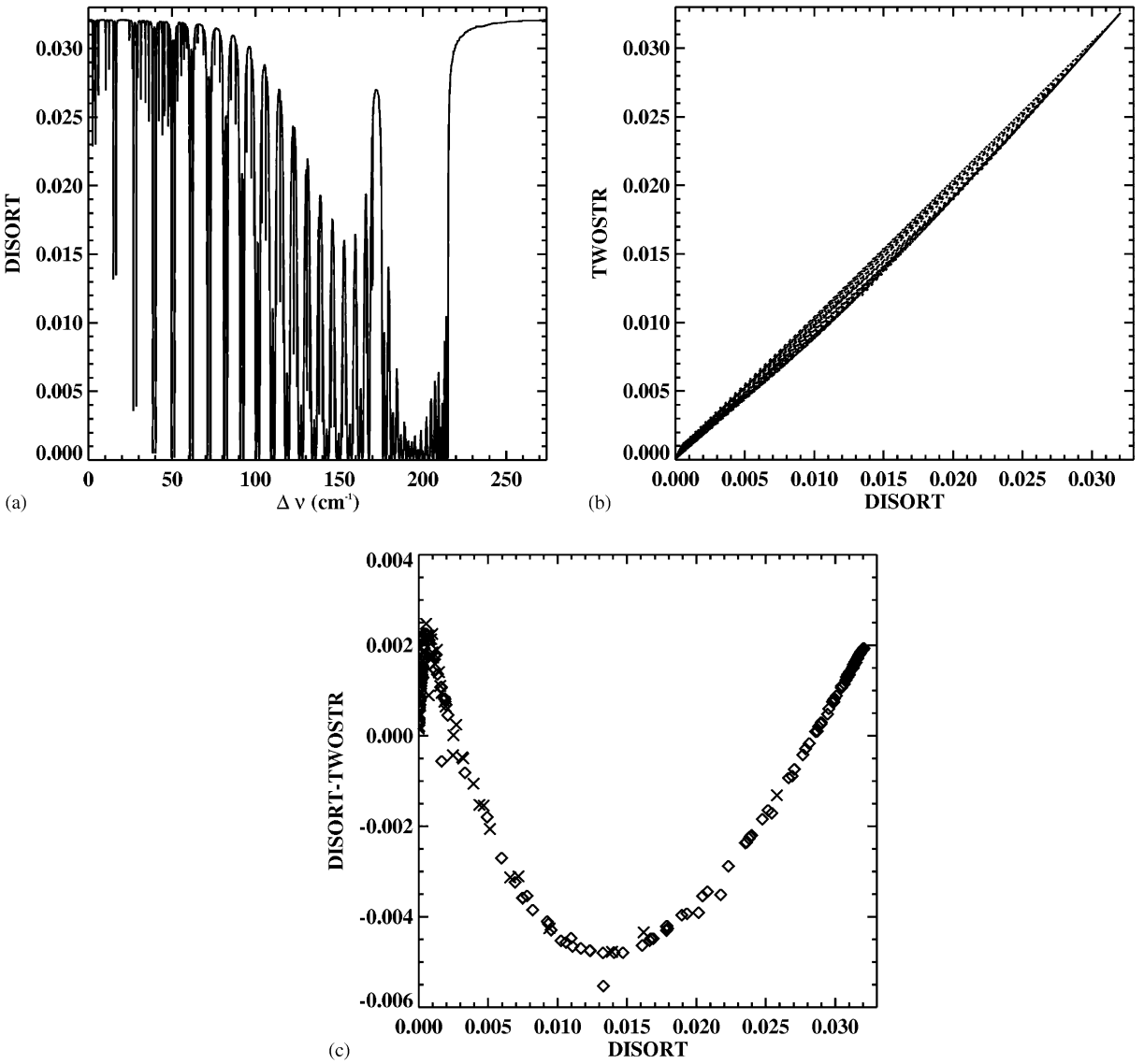

Fig. 1. (a) Upwelling reflectance spectrum at TOA obtained from DISORT, $v(\mathrm{cm}^{-1}) = v_0 + \Delta v$, $v_0 = 12950\,\mathrm{cm}^{-1}$; (b) correlation plot between DISORT and TWOSTR TOA reflectance spectra; (c) difference between TWOSTR and DISORT TOA reflectance spectra. ◇: P branch, ×: R branch. The residuals have been plotted as a function of the DISORT reflectance to show systematic deviations more clearly.

If λ_k is the eigenvalue corresponding to the kth eigenvector, then the scaled EOF $\boldsymbol{\varepsilon}_k$ can be defined as

$$\boldsymbol{\varepsilon}_k = \sqrt{\lambda_k}\boldsymbol{\varphi}_k. \tag{5}$$

Note that the scaled EOFs (hereafter simply referred to as EOFs) have the same dimension as the optical properties and can hence be more easily interpreted than the EOFs. Further, the EOFs are just a new basis to represent the original data, so there is no loss of information provided that a complete

set is used. As will be shown below, a few EOFs are sufficient to reproduce nearly all the information. In practice, PC analysis is performed in logarithmic space for reasons of computational efficiency (see Appendix A for further illustration).

The PCs, $\mathbf{P}_k$, are the projections of the original data set onto the associated EOFs (scaled by the eigenvalue).

$$P_{kl} = \sum_{i=1}^{sM} \frac{\varepsilon_{ki} F_{il}}{\lambda_k}, \tag{6}$$

where ε_{ki} is the ith component of the kth EOF and P_{kl} is the lth component of the kth PC.

The fundamental properties that characterize any radiative transfer problem are the optical depth $d\tau$, the single scattering albedo ω, the surface reflectance and the phase function. We assume for simplicity that the latter two do not vary with wavenumber (although this is not a necessary assumption, the variations are negligible over the width of a molecular absorption band). So, in our analysis, the number of optical properties s considered is *two*. The first M components of each EOF are for the optical depth while components $M+1$ to $2M$ are for the single scattering albedo.

As with spectral mapping techniques, our aim is to reduce the number of radiative transfer calculations by grouping wavenumbers at which the optical properties are similar. The challenge then is to find a way to do the grouping. Fig. 2 shows the layer optical depth and single scattering albedo profiles, with different lines denoting different wavenumbers. It is clear from this figure that the maximum variability in the optical depth occurs in the bottom half of the atmosphere while that of the single scattering albedo is fairly uniform (ignoring very small values which have negligible impact on the reflectance). Keeping this in mind, our grouping criteria are as follows:

- $c_1 < \ln(2\tau_2) < c_2$, where $\tau_2 \equiv \sum_{i=11}^{22} d\tau_i$ is the cumulative optical depth of the lower half of the atmosphere (layers 11–22),
- $c_3 < \omega_1 < c_4$ where ω_1 is the single scattering albedo of the top layer,

where c_1, c_2, c_3 and c_4 are to be picked by the user.

A particular choice of the parameters c_1, c_2, c_3, and c_4 defines a 'case'. In other words, it is a range of optical properties (i.e. a group of wavenumbers) corresponding to a single EOF calculation. The EOFs and PCs are then calculated using Eqs. (5) and (6). With proper case selection, the first few EOFs can capture more than 99% of the total variance. Figs. 3 and 4 show the first *two* EOFs (and the corresponding PCs) for the sample case where $c_1 = 0.25$, $c_2 = 0.5$, $c_3 = 0.7$ and $c_4 = 1$ (in the P branch). The reconstruction of the monochromatic reflectances from the EOFs and PCs is discussed in the following section.

As will be shown in Appendix A, the EOFs reflect the vertical variations in the gas density and the half-width of the spectral lineshape, while the PCs display the dependence of the line shape on frequency. The reason this approach works so well is that any point in a molecular absorption band can be considered to be some part of a strong line (center, near-wing or far-wing) or a combination of the above (due to line overlap); the EOFs for a single strong line thus have all the features expected in the entire band. Indeed, the results indicate that line overlap can be accounted for, to a very good approximation, by a linear combination of the EOFs corresponding to the individual lines.

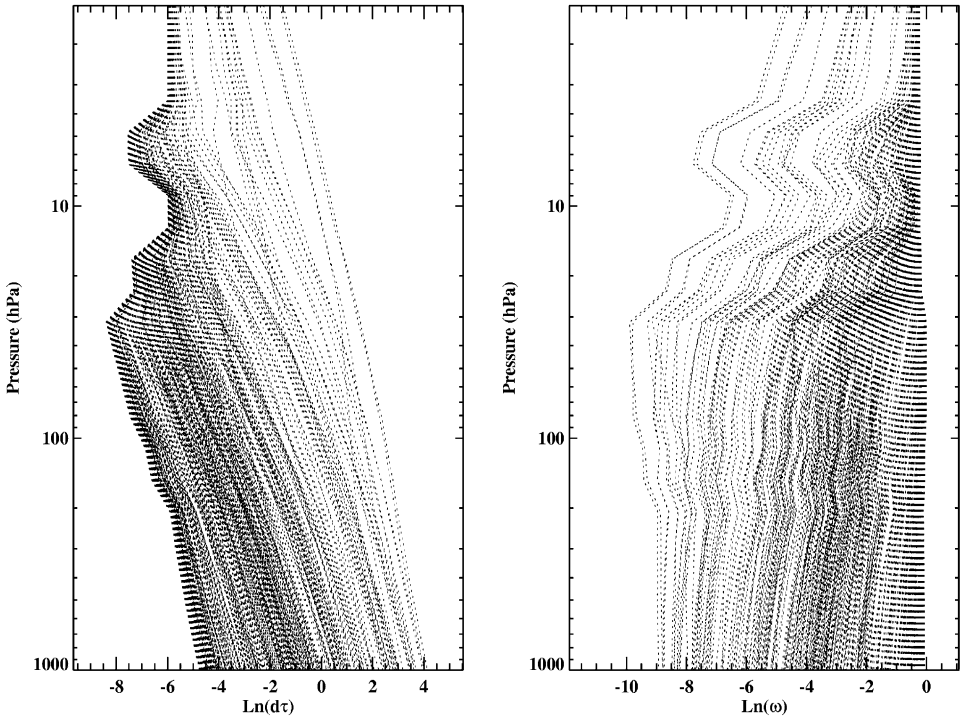

Fig. 2. Layer optical depth ($d\tau$) and single scattering albedo (ω) profiles. The different lines represent different wavenumbers. For clarity of presentation, the profiles are shown only for every 25th wavenumber (pixels 1, 26, 51,..., 10 601).

For each case, the optical depth profile at the wavenumbers associated with that case can be reconstructed from the EOFs and PCs as follows:

$$\ln d\tau_{il} = \overline{\ln d\tau_{il}} + \sum_{k=1}^{2M} P_{kl}\varepsilon_{ki}, \tag{7}$$

where $d\tau_{il}$ is the *total* optical depth of layer i at the lth wavenumber, $M = 22$ and the overbar denotes the mean over all wavenumbers. In practice, three or four terms are enough to reproduce the optical depth to the desired accuracy. A similar procedure can be performed for the single scattering albedo.

5. Mapping to TOA reflectance

For each case, the TOA reflectances are calculated for the mean optical properties associated with that case, using DISORT and TWOSTR. The difference is denoted as I_d. A similar calculation is then done for a perturbation of magnitude one EOF, with the result denoted as $I_d^+(k)$ if the perturbation is positive and $I_d^-(k)$ if the perturbation is negative; k refers to the EOF

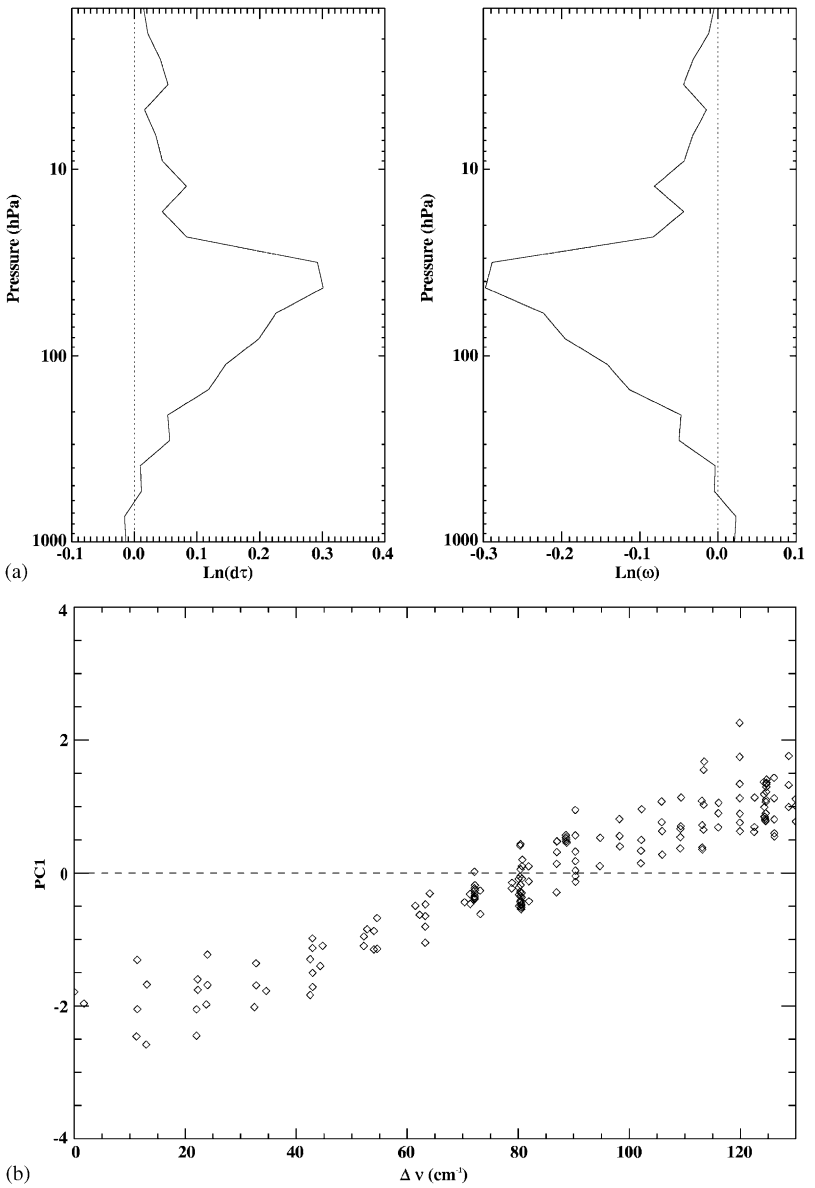

Fig. 3. (a) EOF1: The computed EOF1 has been split into two, corresponding to the layer optical depth ($d\tau$) and single scattering albedo (ω), for ease of visualization; (b) PC1: $v(\mathrm{cm}^{-1}) = v_0 + \Delta v$, $v_0 = 12\,950\,\mathrm{cm}^{-1}$. PC1 shows the deviation of the optical properties (in EOF1 units) from the mean profile.

being considered. The first and second order differences with respect to the EOF, δI_k and $\delta^2 I_k$, respectively, are calculated as follows:

$$\delta I_k = \frac{I_{\mathrm{d}}^{+}(k) - I_{\mathrm{d}}^{-}(k)}{2}, \tag{8}$$

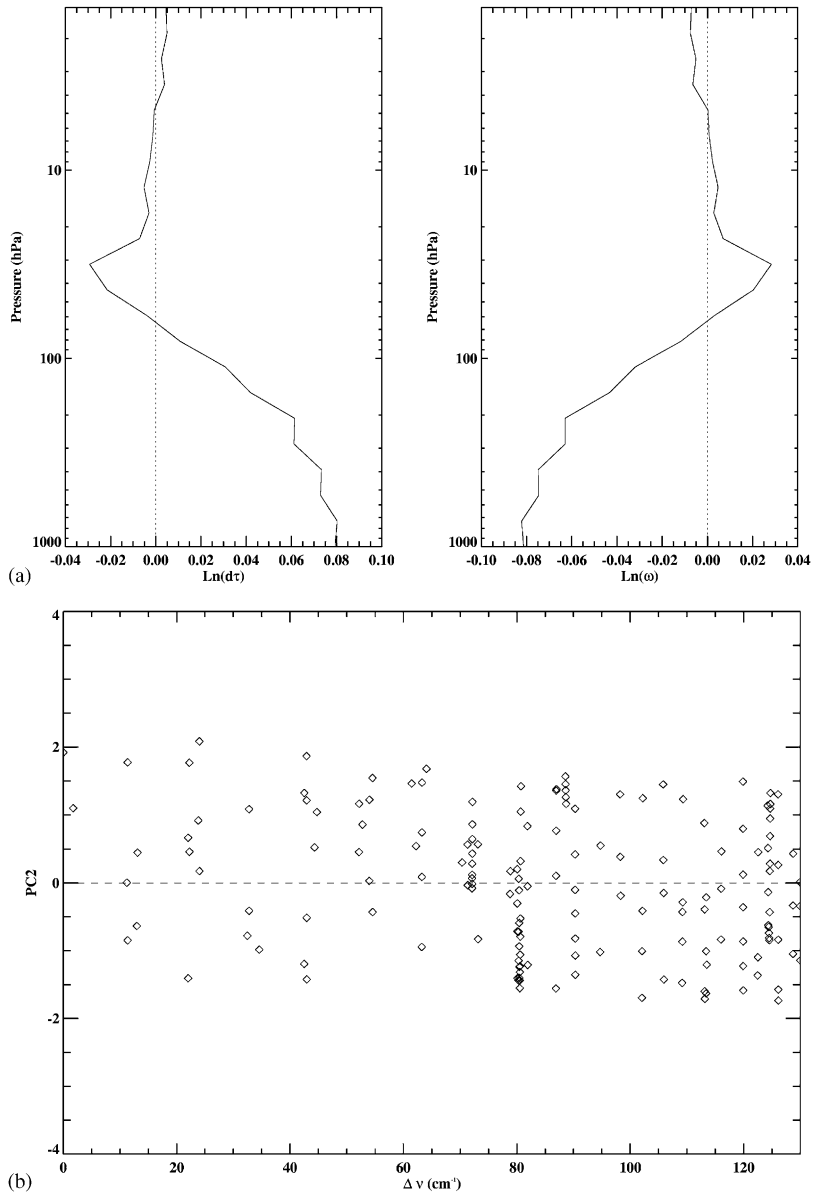

Fig. 4. (a) EOF2: The computed EOF2 has been split into two, corresponding to the layer optical depth ($d\tau$) and single scattering albedo (ω), for ease of visualization; (b) PC2: $v(\mathrm{cm}^{-1}) = v_0 + \Delta v$, $v_0 = 12\,950\,\mathrm{cm}^{-1}$. PC2 shows the deviation of the optical properties (in EOF2 units) from the mean profile.

$$\delta^2 I_k = I_{\mathrm{d}}^{+}(k) - 2I_{\mathrm{d}} + I_{\mathrm{d}}^{-}(k). \tag{9}$$

The TOA reflectance for the lth wavenumber, I_l, is then calculated using

$$I_l = I_l^{\mathrm{TS}} + I_{\mathrm{d}} + \sum_{k=1}^{4} \delta I_k P_{kl} + \frac{1}{2} \sum_{k=1}^{4} \delta^2 I_k P_{kl}^2, \tag{10}$$

where I_l^{TS} is the TOA reflectance for the lth wavenumber, calculated using TWOSTR.

Eq. (10) illustrates why it is better to use the residual between DISORT and TWOSTR reflectances, rather than that computed directly from DISORT, for the PC analysis. The above expansion assumes that the reflectance has a quadratic relationship with the PCs. Clearly, the smaller the variance in the reflectances, the better the approximation would be. We found that *four* EOFs were sufficient to reproduce the reflectance to the accuracy desired. The error in the above three-term expansion is $O(\delta^3 I_k P_{kl}^3)$. By choosing the cases such that the change in the reflectance, for a perturbation in optical properties of magnitude one EOF, is less than a percent, we can keep the error to a few tenths of a percent.

6. Recovering the O_2 *A* band

An error criterion of less than 1.0% was chosen for all but the most saturated lines, to simulate expected results for space-based detection [23]. The total number of monochromatic wavenumber grid points for the radiative transfer calculation was 10 616; only 105 cases were needed to perform the PC analysis. As mentioned in Section 5, for each case a DISORT and a TWOSTR call are made for the mean optical properties and for perturbations of magnitude one EOF (positive and negative) for *each* EOF used to map back to the reflectance. Since we use *four* EOFs to reconstruct the reflectance, a total of $1 + 2 * 4 = 9$ DISORT (and 9 TWOSTR) calls are required for each case. In addition, since the PC analysis is done on the residual between DISORT and TWOSTR reflectances, there is an additional TWOSTR call for every wavenumber to recover the TOA reflectance, as is evident from Eq. (10). However, since the PC analysis and the TWOSTR calculations themselves take negligible time compared to a full multi-stream radiative transfer calculation, this method offers us an order of magnitude improvement in speed.

In the above analysis, very stringent accuracy criteria have been employed. Relaxing that would offer even more savings in computation time. Figs. 5 and 6 show the O_2 *A* band spectra obtained using DISORT and PC analysis, and the residuals. Figs. 7 and 8 show the same spectra after convolution with an instrument line shape that is a sum of Lorentzians. Clearly, the residuals are much smaller after convolution. This implies that the errors from PC analysis are mostly random. Also, the fractional residuals are very close to zero near the continuum and are highest in the center of strong lines, as one would expect.

7. Conclusions

A novel technique based on PC analysis has been introduced to increase the computational efficiency of radiative transfer calculations in an absorbing, scattering atmosphere. It was

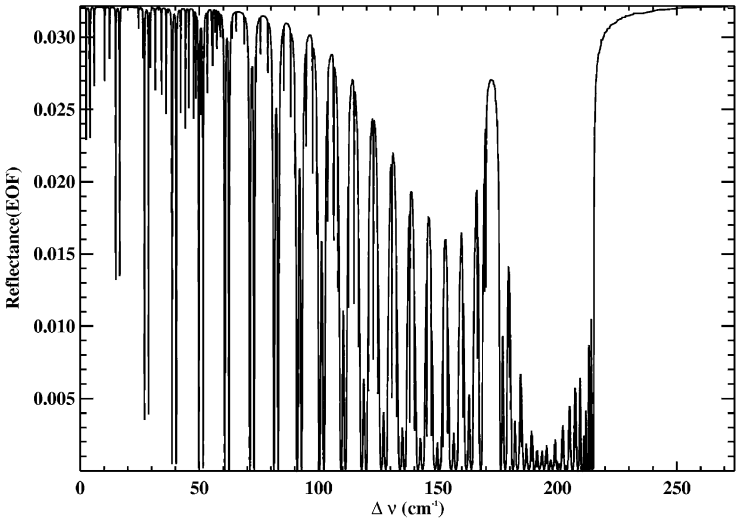

Fig. 5. Reflectance spectrum calculated from PC analysis (high resolution), $v(\mathrm{cm}^{-1}) = v_0 + \Delta v$, $v_0 = 12\,950\,\mathrm{cm}^{-1}$.

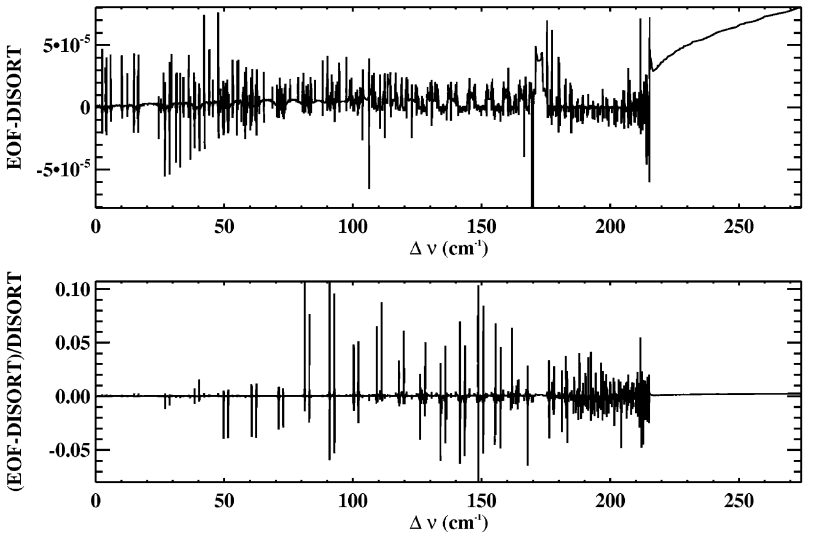

Fig. 6. (Top) residues (high resolution); (bottom) fractional residues (high resolution), $v(\mathrm{cm}^{-1}) = v_0 + \Delta v$, $v_0 = 12\,950\,\mathrm{cm}^{-1}$.

observed that the first few EOFs accounted for most of the variability in the system. Using the optical depth and the single scattering albedo as the EOF parameters, the O_2 *A* band was reproduced using the new technique. Using the correlation between a two-stream and a multi-stream approach, the O_2 *A* band spectrum was reproduced with an accuracy of 0.3% while achieving an order of magnitude speed improvement. The PC method has great potential for use in practical radiative transfer codes and warrants further consideration.

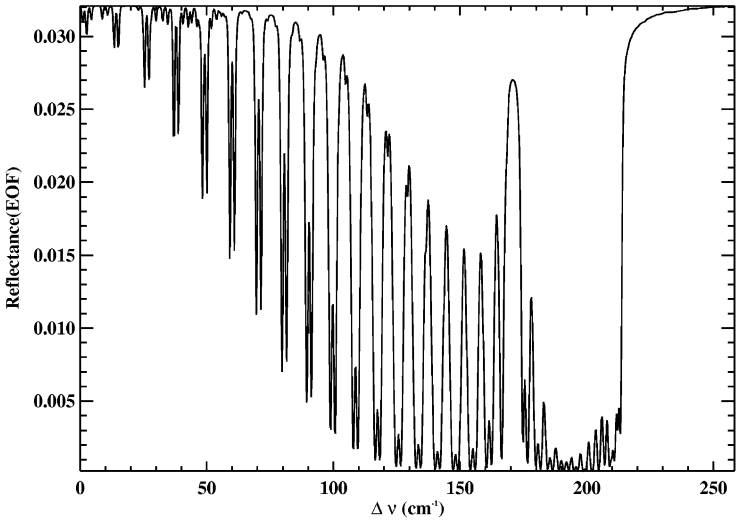

Fig. 7. Reflectance spectrum calculated from PC analysis (after convolution), $v(\mathrm{cm}^{-1}) = v_0 + \Delta v$, $v_0 = 12\,950\,\mathrm{cm}^{-1}$.

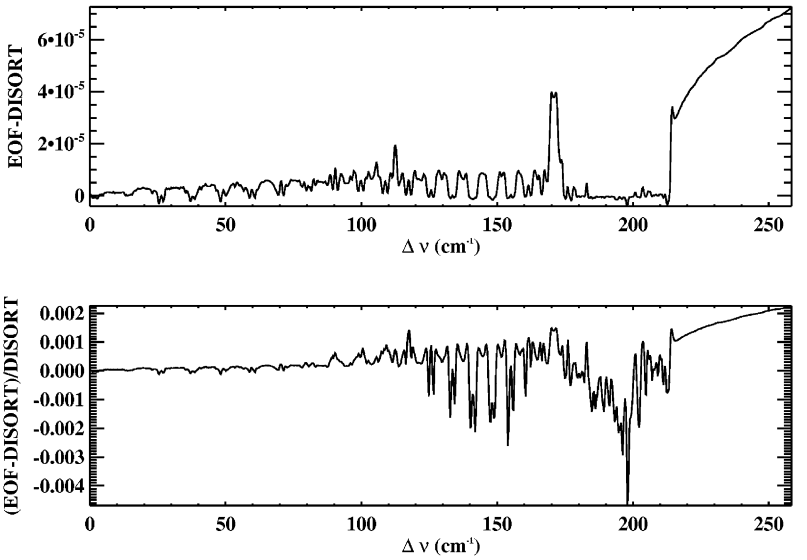

Fig. 8. (Top) residues (after convolution); (bottom) fractional residues (after convolution), $v(\mathrm{cm}^{-1}) = v_0 + \Delta v$, $v_0 = 129\,50\,\mathrm{cm}^{-1}$.

Acknowledgments

This work was supported in part by NASA Grant NAG1-1806 and the Orbiting Carbon Observatory (OCO) Project at JPL.

Appendix A. Principal component analysis of the profiles of optical depth and single scattering albedo for a Lorentzian layer lineshape

Here we apply PC analysis to a highly idealized case. By this simple example, we illustrate the practical reason behind applying PC analysis in logarithmic space and the physical meaning of EOF decomposition of the profiles of spectrally-dependent optical properties.

For a uniformly distributed gas in an isothermal atmosphere, we divide the atmosphere into M layers such that the ith layer has thickness L_i. For simplicity, we assume a Lorentzian line shape for each layer. Then the gas absorption optical depth profile, $d\tau_{il}^{g}$, can be written as

$$d\tau_{il}^{g} = \rho_i L_i S \frac{\alpha_i}{\pi[(v_l - v_0)^2 + \alpha_i^2]}, \tag{A.1}$$

where i denotes the ith layer from the surface, l denotes the lth spectral point, ρ_i is the gas density in the ith layer, S is the line strength, α_i is the half-width of the Lorentzian line shape in the ith layer, and $v_l = l\Delta + v_0$, where v_0 is the wavenumber of the line center and Δ is the wavenumber grid spacing. If we approximate the mean pressure of each layer by the pressure at the mid-point of the layer, then we have

$$P_i = P_0 \exp\left[-\left(i - \tfrac{1}{2}\right) L_i / H\right], \tag{A.2}$$

$$\rho_i = \rho_0 \exp\left[-\left(i - \tfrac{1}{2}\right) L_i / H\right], \tag{A.3}$$

$$\alpha_i = \alpha_0 \exp\left[-\left(i - \tfrac{1}{2}\right) L_i / H\right], \tag{A.4}$$

where P_i is the mean pressure in layer i, H is the scale height (which is a constant for an isothermal atmosphere), and subscript 0 denotes the surface. Substituting (A.3) and (A.4) into (A.1), we have

$$d\tau_{il}^{g} = \frac{\rho_0 \alpha_0 L_i S}{\pi} \left(\frac{l^2 \Delta^2}{\exp[-(2i-1) L_i / H]} + \alpha_0^2 \right)^{-1}. \tag{A.5}$$

Ignoring the correction factor for anisotropy, the Rayleigh scattering optical depth profile, $d\tau_{il}^{s}$, can be written as

$$d\tau_{il}^{s} = \sigma_l n_i L_i, \tag{A.6}$$

where σ_l is the Rayleigh scattering cross section at v_l and n_i is the number density in the ith layer. At the NIR and visible spectral regions, for a single absorption line, $l\Delta \ll v_0$; therefore, we can simply treat σ_l as constant, σ_0. For example, based on Bates' formula [24], the difference between the Rayleigh scattering cross sections at 12949 and 12951 cm^{-1} is only 0.04%. The single

scattering albedo can then be written as

$$\begin{aligned}\omega_{ij} &= \frac{\mathrm{d}\tau_{il}^{s} + \mathrm{d}\tau_{il}^{\mathrm{a}}}{\mathrm{d}\tau_{il}^{\mathrm{g}} + \mathrm{d}\tau_{il}^{s} + \mathrm{d}\tau_{il}^{\mathrm{a}}} \\ &= \frac{\sigma_0(\rho_i/\overline{M})N_{\mathrm{A}}L_i + \mathrm{d}\tau_{il}^{\mathrm{a}}}{\rho_i L_i S(\alpha_i/\pi[(v_l - v_0)^2 + \alpha_i^2]) + \sigma_0(\rho_i/\overline{M})N_{\mathrm{A}}L_i + \mathrm{d}\tau_{il}^{\mathrm{a}}} \\ &= \left(\frac{\overline{M}\rho_i L_i S}{\sigma_0\rho_i L_i N_{\mathrm{A}} + \mathrm{d}\tau_{il}^{\mathrm{a}}\overline{M}}\,\frac{\alpha_i}{\pi[(v_l - v_0)^2 + \alpha_i^2]} + 1\right)^{-1}, \end{aligned} \tag{A.7}$$

where $\mathrm{d}\tau_{il}^{\mathrm{a}}$ is the aerosol scattering optical depth profile, N_{A} is the Avogadro number, and $\overline{M}$ is the molar mass of air. The aerosols are assumed to be purely scattering, which is a good approximation for aerosols like sulfate. Putting the single scattering albedo and the total optical depth together, we have

$$\mathbf{X}_{il} = \begin{pmatrix} \dfrac{\rho_0\alpha_0 L_i S}{\pi}\left(\dfrac{l^2\Delta^2}{(P_i/P_0)^2} + \alpha_0^2\right)^{-1} + \dfrac{\sigma_0\rho_0 N_{\mathrm{A}} L_i}{\overline{M}}(P_i/P_0) + \mathrm{d}\tau_{il}^{\mathrm{a}} \\ \left(\dfrac{\overline{M}\rho_0(P_i/P_0)L_i S}{\pi(\sigma_0\rho_0(P_i/P_0)LN_{\mathrm{A}} + \mathrm{d}\tau_{il}^{\mathrm{a}}\overline{M})}\,\dfrac{\alpha_0 P_i/P_0}{l^2\Delta^2 + \alpha_0^2(P_i/P_0)^2} + 1\right)^{-1} \end{pmatrix}, \tag{A.8}$$

where $\mathbf{X}$ is the matrix for which PC analysis is to be performed, $i = 1, 2, 3, \ldots, M$ and $l = -N, \ldots, -2, -1, 0, 1, 2, \ldots, N$. Each element of $\mathbf{X}$ is a 2-dimensional vector, the two components being the layer optical depth and single scattering albedo, respectively. The columns of $\mathbf{X}$ show the variations of the gas density and the Lorentzian line shape with altitude; the rows show the dependence of the Lorentzian line shape on frequency.

The following reasonable values are assigned to the parameters involved in the problem: $\rho_0 = 1.29\,\mathrm{kg/m^3}$, $\alpha_0 = 0.1\,\mathrm{cm^{-1}}$, $S = 0.00223\,\mathrm{cm/g}$ (strong line in the O_2 A band), $\Delta = 0.005\,\mathrm{cm^{-1}}$,

Table 2
The fractions of variance and the cumulative fractions of variance explained by six leading EOFs when PC analysis is applied to $\mathbf{X}$ in real space and in logarithmic space

	PC analysis on X		PC analysis on $\ln(X)$	
	Fraction of variance	Cumulative fraction of variance	Fraction of variance	Cumulative fraction of variance
EOF1	7.96536×10^{-1}	7.96536×10^{-1}	8.81154×10^{-1}	8.81154×10^{-1}
EOF2	1.23927×10^{-1}	9.20463×10^{-1}	1.10397×10^{-1}	9.91551×10^{-1}
EOF3	5.65170×10^{-2}	9.76980×10^{-1}	7.66840×10^{-3}	9.99219×10^{-1}
EOF4	1.80746×10^{-2}	9.95055×10^{-1}	7.25571×10^{-4}	9.99945×10^{-1}
EOF5	3.79672×10^{-3}	9.98851×10^{-1}	3.09480×10^{-5}	9.99976×10^{-1}
EOF6	9.27283×10^{-4}	9.99779×10^{-1}	2.16236×10^{-5}	9.99997×10^{-1}

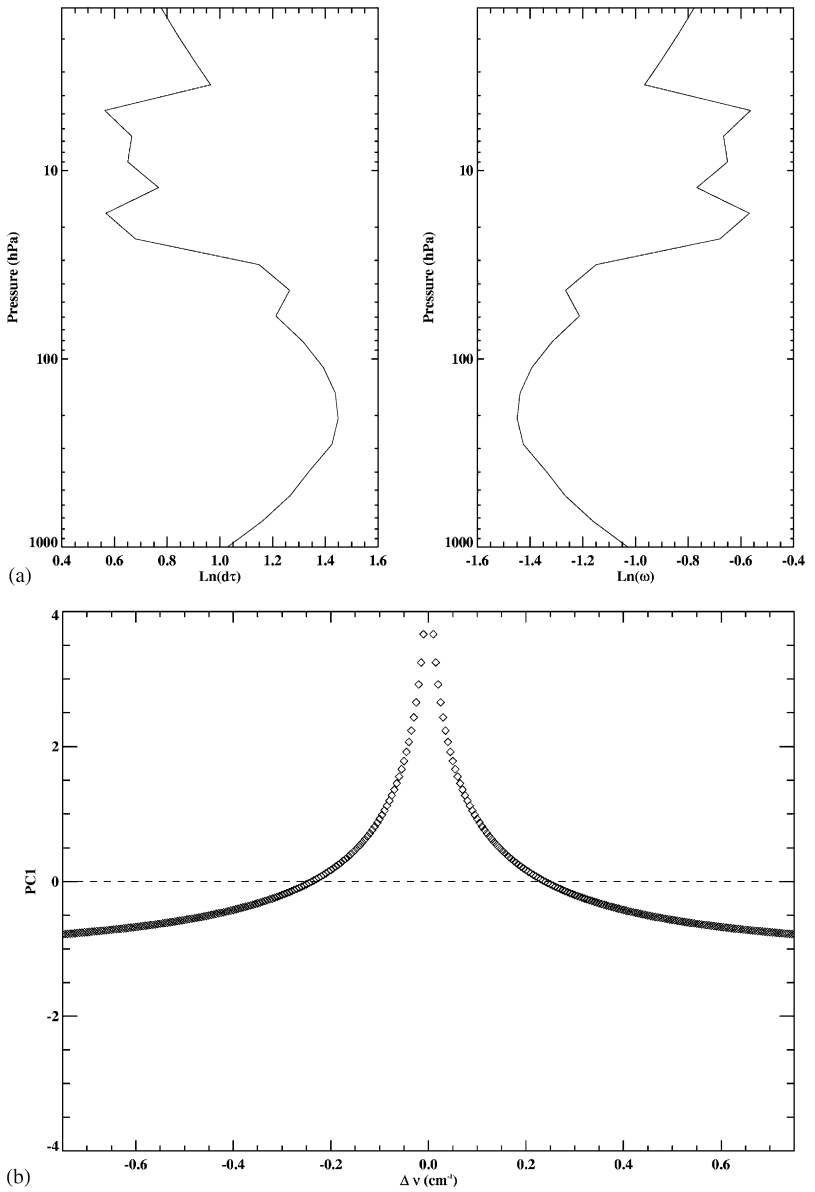

Fig. 9. (a) EOF1: The computed EOF1 has been split into two, corresponding to the layer optical depth ($d\tau$) and single scattering albedo (ω), for ease of visualization; (b) PC1: $(\mathrm{cm}^{-1}) = v_0 + \Delta v$, v_0 (line center wavenumber) = $13001.70984\,\mathrm{cm}^{-1}$. PC1 shows the deviation of the optical properties (in EOF1 units) from the mean profile.

$P_0 = 1000\,\mathrm{hPa}$, $\sigma_0 = 1.1 \times 10^{-27}\,\mathrm{cm}^2$, $\overline{M} = 29\,\mathrm{g/mol}$, $M = 22$ and $N = 150$. The pressure profile is obtained from Table 1 and the altitude profile by then using the hydrostatic equation ($H = 8\,\mathrm{km}$). Note that subscript 0 here refers to the surface but in Table 1, it refers to the TOA. The aerosol scattering optical depth profile is the same as that used in the O_2 A band PC analysis.

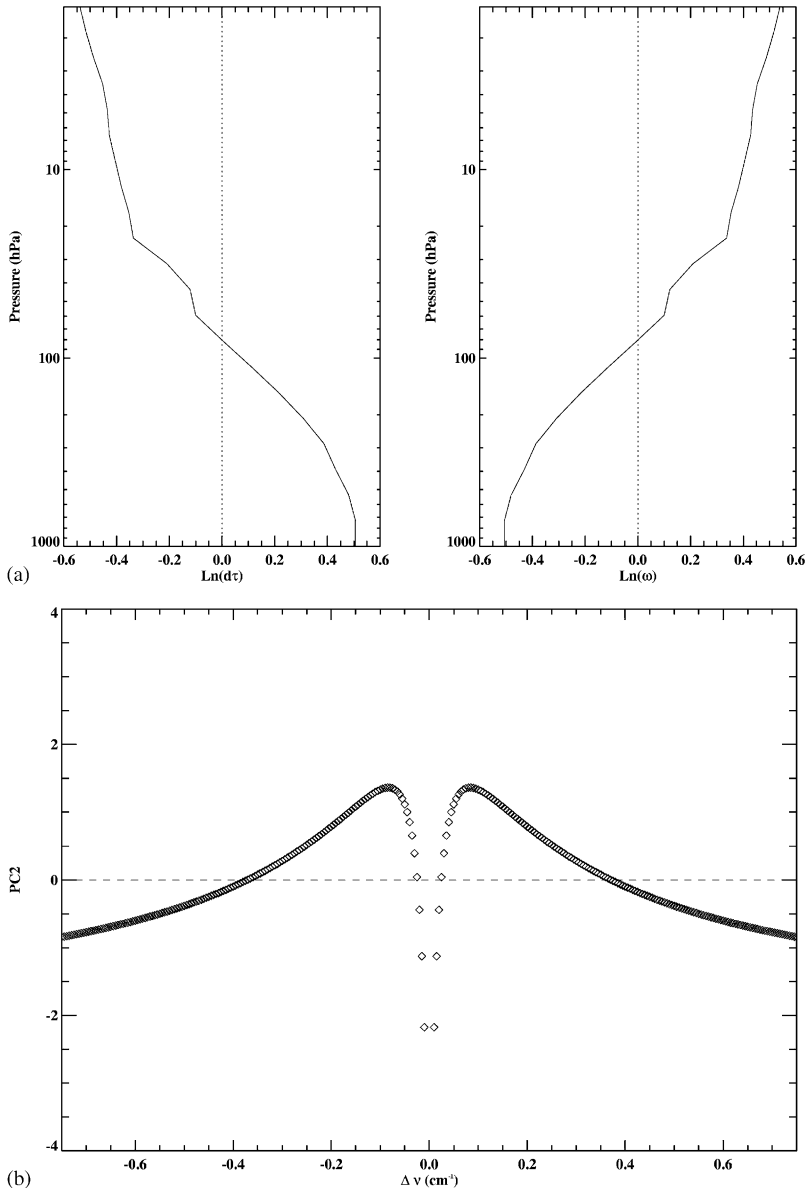

Fig. 10. (a) EOF2: The computed EOF2 has been split into two, corresponding to the layer optical depth ($d\tau$) and single scattering albedo (ω), for ease of visualization; (b) PC2: $v(\mathrm{cm}^{-1}) = v_0 + \Delta v$, $v_0 = 13001.70984\,\mathrm{cm}^{-1}$. PC2 shows the deviation of the optical properties (in EOF2 units) from the mean profile.

The fractions of variance, as well as the cumulative fractions of variance, explained by the 6 leading EOFs are listed in Table 2. The first EOF is absolutely dominant in the variance. Six leading EOFs together can explain more than 99.999% of the total variance.

If we apply PC analysis to the column vectors of $\ln(\mathbf{X})$ instead of $\mathbf{X}$, then the *three* leading EOFs can explain 99.92% of the total variance, very close to the amount of variance explained by the *six*

leading EOFs when the analysis is applied to **X**. Therefore, fewer EOFs are needed in logarithmic space than in real space to capture the same fraction of the total variance. This is because the variance of $\mathbf{X}_{il}$ could be very large in the real space: for a given layer, from the line wing ($l = \pm N$) to the line center ($l = 0$), the values of $\mathbf{X}_{il}$ could differ by as much as three orders of magnitude. In the logarithmic space, the variance of $\mathbf{X}_{il}$ would not be that large: the difference between the maximum and minimum of $\mathbf{X}_{il}$ is still within one order of magnitude. Accuracy of the reconstructed profiles is directly related to the fraction of the total variance captured by the leading EOFs used in the reconstruction. Therefore, given the extremely heavy computational load in practical retrievals and required accuracy for forward radiative modeling, doing PC analysis and reconstruction in logarithmic space is more efficient than doing them in real space.

The leading *two* EOFs and the corresponding PCs derived from the PC analysis of **X** in logarithmic space are plotted in Figs. 9 and 10. The PCs have zero mean and unitary standard deviations. Remarkably, the EOFs (Figs. 9a and 10a) retain the features obtained in the full-band EOFs (Figs. 3a and 4a). This indicates that a single strong line captures all the features of an entire molecular absorption band. The corresponding PCs are symmetric with respect to the line center and the line center is the global minimum/maximum for all PCs. Besides the global maximum at the line center, PC1 (Fig. 9b) has no local minimum and maximum while PC2 (Fig. 10b) has two local maxima symmetric to the line center minimum.

In summary, as far as the accuracy of reconstructing optical properties is concerned, PC analysis and reconstruction in logarithmic space is more computationally efficient than in real space. In this highly simplified case, the results obtained from PC analysis mainly reflect the variations of the gas density and the Lorentzian half-width with respect to altitude, as well as the dependence of the Lorentzian line shape on frequency.

References

[1] Kuang ZM, Margolis JS, Toon GC, Crisp D, Yung YL. Spaceborne measurements of atmospheric CO_2 by high-resolution NIR spectrometry of reflected sunlight: an introductory study. Geophys Res Lett 2002;29(15):1716–9.
[2] Liou KN. An introduction to atmospheric radiation. Amsterdam: Academic Press; 2002.
[3] Ambartzumian V. The effect of the absorption lines on the radiative equilibrium of the outer layers of the stars. Publ Obs Astron Univ Leningrad 1936;6:7–18.
[4] Kondratyev KY. Radiation in the atmosphere. San Diego: Academic Press; 1969.
[5] Yamamoto G, Tanaka M, Asano S. Radiative transfer in water clouds in the infrared region. J Atmos Sci 1970;27:282–92.
[6] Arking AA, Grossman K. The influence of line shape and band structure on temperatures in planetary atmospheres. J Atmos Sci 1972;29:937–49.
[7] Lacis AA, Hansen JE. A parameterization for the absorption of solar radiation in the Earth's atmosphere. J Atmos Sci 1974;31:118–33.
[8] Lacis A, Wang WC, Hansen JE. Correlated *k*-distribution method for radiative transfer in climate models: application to effect of cirrus clouds on climate. NASA Conf Publ 1979;2076:309–14.
[9] Goody RM, West R, Chen L, Crisp D. The correlated-*k* method for radiation calculations in nonhomogeneous atmospheres. JQSRT 1989;42:539–50.
[10] Lacis AA, Oinas V. A description of the correlated *k*-distribution method for modeling nongray gaseous absorption, thermal emission, and multiple scattering in vertically inhomogeneous atmospheres. J Geophys Res 1991;96:9027–63.

[11] Fu Q, Liou KN. On the correlated *k*-distribution method for radiative transfer in nonhomogeneous atmospheres. J Atmos Sci 1992;49:2139–56.
[12] Stam DM, de Haan JF, Hovenier JW, Stammes P. A fast method for simulating observations of polarized light emerging from the atmosphere applied to the oxygen *A* band. JQSRT 2000;64:131–49.
[13] West R, Crisp D, Chen L. Mapping transformations for broadband atmospheric radiation calculations. JQSRT 1990;43:191–9.
[14] Meadows VS, Crisp D. Ground-based near-infrared observations of the Venus nightside: the thermal structure and water abundance near the surface. J Geophys Res 1996;101(E2):4595–622.
[15] Mitchell RM, O'Brien DM. Error estimates for passive satellite measurement of surface pressure using absorption in the *A* band of oxygen. J Atmos Sci 1987;44(15):1981–90.
[16] O'Brien DM, Mitchell RM. Error estimates for retrieval of cloud-top pressure using absorption in the *A* band of oxygen. J Appl Meteorol 1992;31(10):1179–92.
[17] Rothman LS, et al. The HITRAN molecular spectroscopic database: edition of 2000 including updates through 2001. JQSRT 2003;82:5–44.
[18] Stamnes K, Tsay SC, Wiscombe W, Jayaweera K. Numerically stable algorithm for discrete-ordinate-method radiative transfer in multiple scattering and emitting layered media. Appl Opt 1988;27(12):2502–9.
[19] Kylling A, Stamnes K, Tsay SC. A reliable and efficient two-stream algorithm for spherical radiative transfer: documentation of accuracy in realistic layered media. J Atmos Chem 1995;21:115–50.
[20] Huang XL, Farrara L, Leroy SS, Yung YL, Goody RM. Cloud variability as revealed in outgoing infrared spectra: comparing model to observation with spectral EOF analysis. Geophys Res Lett 2002;29(8):1270–3.
[21] Camp CD, Roulston MS, Yung YL. Temporal and spatial patterns of the interannual variability of total ozone in the tropics. J Geophys Res 2003;108(D20):4643–59.
[22] Peixoto JP, Oort AH. Physics of climate. New York: American Institute of Physics; 2002. p. 67–9, 492–5.
[23] O'Brien DM, Mitchell RM, English SA, da Costa GA. Airborne measurements of air mass from O_2 *A* band absorption spectra. J Atmos Ocean Tech 1998;15(6):1272–86.
[24] Bates DR. Rayleigh scattering by air. Planet Space Sci 1984;32:785–90.